Cytometry
PART A
Journal of the
International Society for
Advancement of Cytometry

Three-Dimensional Intracellular Transport in Neuron Bodies and Neurites Investigated by Label-Free Dispersion-Relation Phase Spectroscopy

Mikhail E. Kandel,[1] Daniel Fernandes,[1] Alison M. Taylor,[1,2] Haadi Shakir,[3] Catherine Best-Popescu,[3] Gabriel Popescu[1,3]*

International Society for Advancement of Cytometry

● **Abstract**
Due to the limitations of fluorescence imaging techniques, the study of intracellular cargo is typically restricted to two-dimensional analyses. To overcome low light levels and the risk of phototoxicity, we employ quantitative phase imaging, a family of full-field imaging techniques that measure the optical path length shift introduced by the specimen. Specifically, we use spatial light interference microscopy (SLIM) to study the transport of mass in whole tomographic volumes and show that a time-correlation technique, dispersion-relation phase spectroscopy (DPS), can be used to simultaneously assay the horizontal and vertical traffic of mass through a cell. To validate our method, we compare the traffic inside cell bodies and neuronal extensions, showing that the vertical transport of mass may prove a more sensitive and interesting metric than similar measurements limited to a 2D, horizontal plane.   © 2017 International Society for Advancement of Cytometry

● **Key terms**
intracellular vesicular traffic; quantitative phase imaging; tomography; microscopy; dynamic light scattering; interferometric imaging

Live cells exhibit complex mass transport mechanisms that are spatiotemporally scale-dependent (1). This transport is achieved through passive, diffusion driven, as well as active, molecular motor driven, phenomena. Traditionally, intracellular traffic has been studied using time-lapse fluorescence imaging. Fluorescence correlation spectroscopy was developed to probe the diffusion coefficients at particular points in space (2,3). Later, this approach was generalized to cover the dynamic behavior at a range of spatial scales (4–6). It is known that fluorescence techniques provide valuable molecular specificity, a capability that, unfortunately, comes with limitations of photobleaching and phototoxicity, as well as low light levels. Interestingly, the photobleaching effect can be exploited to extract information about the diffusion of various molecular species (7).

Quantitative phase imaging (QPI) is an emerging field that provides a label-free alternative to studying morphology and dynamics in cellular systems (8). QPI yields an optical path difference map associated with the specimen of interest and, as such, it is sensitive to both local thickness and the refractive index of the sample. Time-lapse QPI informs about both cell membrane fluctuations (9,10) and intracellular mass transport (11–13).

Dispersion-relation phase spectroscopy (14) was developed as an accompanying analysis method for QPI, which is capable of characterizing both the diffusive (random) and active (deterministic) components and retrieving the spatial scales at which each is dominant. So far, to our knowledge, DPS has been applied only to 2D

time series. In this article, we apply DPS, to time-resolved tomograms obtained by full-field white-light QPI. We report the results in terms of diffusion coefficients and spread of advection velocities in low-density neural networks. We found statistically significant differences between transport in the somas (neuron bodies) vs. neurites and longitudinal vs. transverse traffic.

METHODS

Sample Preparation

As described in (15), cortical neurons were cultured and maintained from early postnatal mice (P0-P1, C57BL/6). All animal procedures were carried out in accordance with approved protocols from the Institutional Animal Care and Use Committees (IACUC) at the University of Nebraska Medical Center and the University of Illinois at Urbana-Champaign, in accordance with the recommendations in the Guide for the Care and Use of Laboratory Animals of the National Institutes of Health (Animal Assurance PHS: # A3294-01, Protocol Number: 10-033-08-EP). Frozen neurons were rapidly thawed at 37°C. Following (16) neurons were plated on poly-D-lysine-coated 35 mm glass Petri dishes at a low density ($\sim$65 cells per mm^2) and grown at 37°C, in the presence of 5% CO_2, in standard maintenance media containing Neurobasal® supplemented with B-27 (Invitrogen, Waltham, Massachusetts, USA), 1% 200 mM glutamine (Invitrogen) and 1% penicillin/streptomycin (Invitrogen). Half the media was aspirated bi-weekly and replaced with fresh maintenance media warmed to 37°C. Live imaging studies took place after 3 and days in vitro.

Microscopy

Time-lapse quantitative phase tomograms were acquired every 60 s for 30-min intervals using a Cell Vista SLIM Pro module (Phi Optics, Inc., Champaign, Illinois, USA) coupled to a Zeiss Z1 microscope (63 × /1.4 NA objective). The imaging system is presented in Figure 1 and the SLIM technique is described in more detail in Ref. 17.

A hallmark of this approach is our ability to use the high performance optical assembly of a commercial microscope, essentially to achieving the same diffraction-limited resolution as the underlying optical system. The expected transverse resolution of our system is $1.22\lambda/(NA_c + NA_{Ob}) = 0.34\,\mu$m, which is compatible with the maximum frequency detected in our analysis, $1/0.29\,\mu m^{-1}$.

A volume of $142 \times 106 \times 6.5\,\mu m^3$ was selected to conserve hard disk space, although, in principle, it is possible to acquire larger fields of view (similar challenges are discussed in Ref. 18). At present, each z-slice slice in the tomographic volume takes approximately 170 ms to acquire. Of this time, 90 ms is used to move the piezo focus, while each of the four frames is allowed a 10 ms SLM stabilization period followed by 10 ms of exposure. Owing to our software implementation, and six Samsung 840 SSDs configured in RAID0, writing files to the hard disk is completely masked by the acquisition process.

Once assembled, the tomographic phase data occupied approximately 2 TB of space. To account for drifts in the stage and focus, the time-lapse tomograms were registered using MATLAB™. The aligned data are manually segmented into regions of interests, corresponding to neuron bodies and neurites (Fig. 2). In total, 94 bodies and 138 neurites were evaluated, across three 35 mm dishes imaged over the course
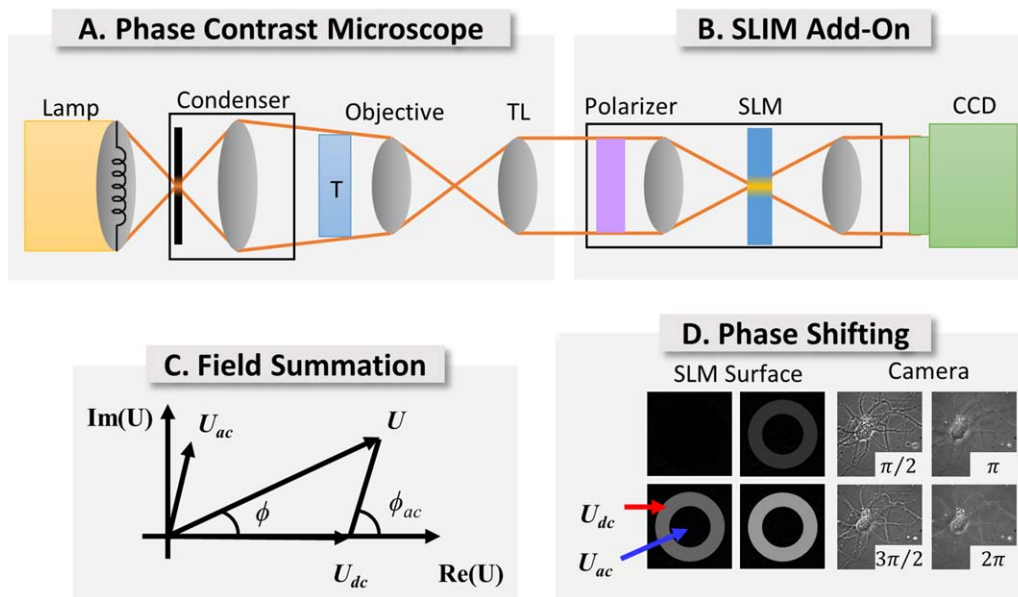

Figure 1. Imaging system. The SLIM add-on (**B**) enhances a phase contrast microscope (**A**) by measuring the phase-shift associated with the object transmission function. As in phase contrast, the total field on the detector (U) is a superposition of the transmitted (Udc) and sample perturbed fields (Uac) (**C**). In our design, a phase ring is matched to an external pupil plane (**D**), and Uac is modulated in $\pi/2$ increments by a spatial light modulator (SLM). From four such images, we recover the phase shift due to the object (ϕ). [Color figure can be viewed at wileyonlinelibrary.com]
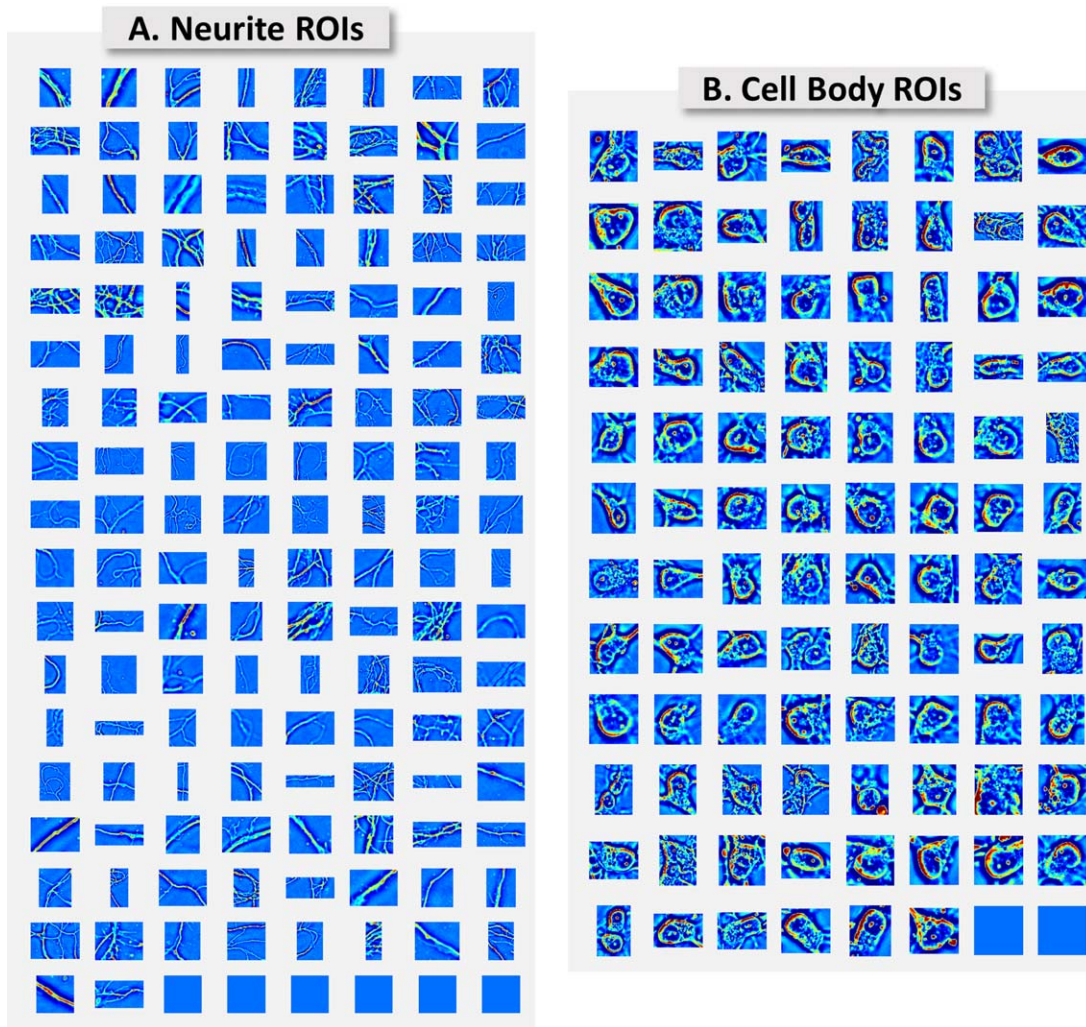
Dispersion-Relation Phase Spectroscopy in 3D

Figure 2. Regions of interest used for analysis, neurites (**A**) and cell bodies (**B**). Raw SLIM data, consisting of time-lapse tomographic phase volumes, were aligned through time using MATLAB™, and the 3D time-series was manually segmented into the two categories. The center of the ROI at the first time point is shown. The scale bar is different for each tile. [Color figure can be viewed at wileyonlinelibrary.com]

of a 2-day period. After the ROIs were located, the system ran without supervision.

Dispersion-Relation Phase Spectroscopy (DPS)

To characterize mass transport, we perform dispersion-relation phase spectroscopy (14). This method of analysis yields a relationship between the temporal bandwidth fluctuations and the diffusion/advection coefficients characterizing the mass flow (Fig. 3). These parameters measure the degree of random and directed motion, and the spatial scales at which each is dominant. Here the mass density, $\eta(\boldsymbol{q}, t)$, is assumed to follow the diffusion-advection equation, namely

$$\left(-Dq^2 + i\boldsymbol{q}\cdot\boldsymbol{v} - \frac{\partial}{\partial t}\right)\eta(\boldsymbol{q}, t) = 0 \qquad (1)$$

where D is the diffusion coefficient, and v is the velocity of directed motion. Following the derivation in Ref. 19, the autocorrelation of the imaging field becomes:

$$\langle g(\boldsymbol{q}, \tau)\rangle_{\boldsymbol{v}} = \exp\left(iqv_0\tau\right)\exp\left[-\left(Dq^2 + \Delta vq\right)\tau\right] \qquad (2)$$

where $\langle g(\boldsymbol{q}, \tau)\rangle_{\boldsymbol{v}}$ is the *spatial* Fourier transform of the temporal autocorrelation and $\langle\rangle_{\boldsymbol{v}}$ indicates ensemble averaging over the velocity distribution. Here, v_0 is the mean velocity and Δv represents the variance of the velocity distribution. As the sample is stationary, v_0 is typically negligible over the field view. Furthermore, the volumes are digitally aligned before computation *ensuring* that this value is minimal. It is worth stressing that our 3D acquisition is robust to "focus drift" defects that otherwise perturb 2D dynamic light scattering measurements.

Thus, the decay at each spatial frequency, $\Gamma(q)$, can be used to characterize the behavior of the sample,

$$\Gamma(q) = Dq^2 + \Delta vq. \qquad (3)$$

To obtain a tractable expression for Γ, we note that Γ is the standard deviation of the power spectrum;

A. Step 1: Data Acquisition

T=0 min   T=1   T=N

B. Step 2: Fourier Transform

T=0 min   T=1   T=N

C. Step 3: Bandwidth Estimation

$\Gamma(qx,qy,qz)$ $\Gamma xy(qz=0)$ $\Gamma yz(qx=0)$

D. Step 4: Parameter Extraction

Γ (rad/s)

λ_{max} λ_{min}
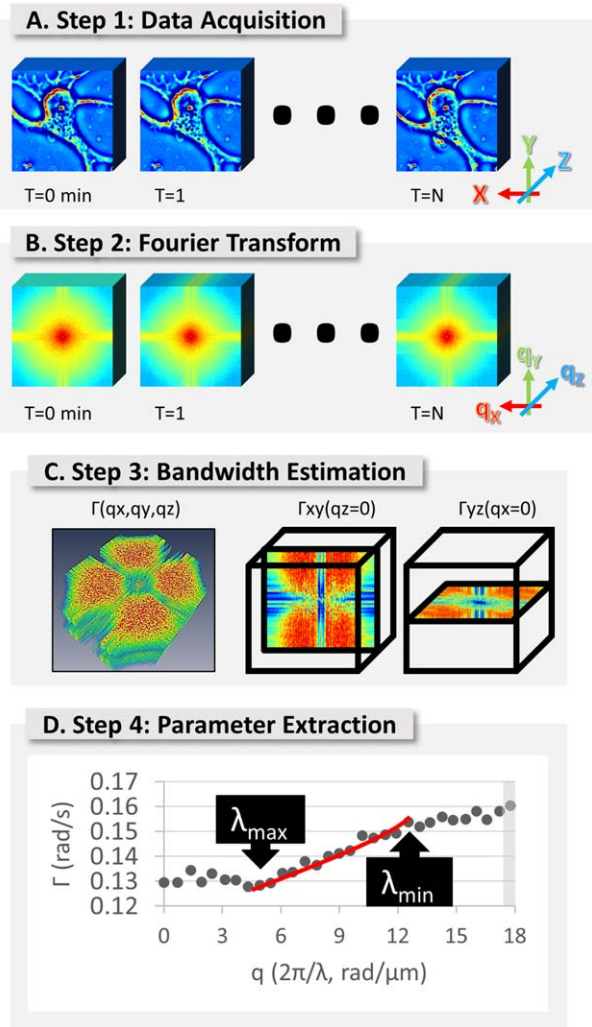
q ($2\pi/\lambda$, rad/μm)

Figure 3. Dispersion relation calculated from the bandwidth of the Fourier transformed volumes. The DPS transport assay consists of four steps. First, time-lapse tomograms are acquired, the Fourier transform is taken of each volume (**A**). To estimate the dispersion relation at each spatial mode (**B**), we perform a forward difference which reduces the 3D data to a single cube. This cube is then reduced to two lines by taking the radial average along the XY and YZ dimensions (**C**), yielding relations for horizontal and vertical motion (**D**). [Color figure can be viewed at wileyonlinelibrary.com]

$$\Gamma^2 = \langle \omega^2 \rangle - \langle \omega \rangle^2 \qquad (4)$$

For most samples the mass transport is equally probable in both directions, the average frequency is zero, $\langle \omega \rangle = 0$, and the second moment can be written as (20):

$$\Gamma^2(q) = \frac{\int \omega^2 |g(\boldsymbol{q}, \omega)|^2 d\omega}{\int |g(\boldsymbol{q}, \omega)|^2 d\omega} \qquad (5)$$

where $g(\boldsymbol{q}, \omega)$ is the Fourier transform of $g(\boldsymbol{q}, t)$ along the temporal dimension. The integral on the right-hand side, can be calculated in the time domain as:

$$\Gamma^2(q) = \frac{\int \left| \frac{dg(\boldsymbol{q},t)}{dt} \right|^2 dt}{\int |g(\boldsymbol{q}, t)|^2 dt} \qquad (6)$$

An interesting feature of this expression is the implicit correction (deconvolution) of the microscope's time-invariant 3D point-spread function [PSF($\boldsymbol{q}$)],

$$\Gamma^2(q) = \frac{\int \left| \text{PSF}(\boldsymbol{q}) \frac{dg(\boldsymbol{q},t)}{dt} \right|^2 dt}{\int |\text{PSF}(\boldsymbol{q}) g(\boldsymbol{q}, t)|^2 dt}. \qquad (7)$$

Thus, the dispersion relation can be calculated by, essentially, differencing along the time axis the spatial Fourier transform of the time series volumes, $g(\boldsymbol{q}, t)$ (Fig. 3b).

To distinguish between transport along horizontal from transport along the vertical axes, the data is separated into *XY* ("transverse") and *YZ* ("medial") planes (Fig. 3c). Under the assumption of anisotropic transport, a radial average is performed to reduce each 2D plane into a 1D line. The slope of this line recovers separate D and Δv coefficients for *XY* and *YZ* mass flow, reducing four-dimensional data into four numbers.

SPATIAL SCALES

Due to the diversity of transport phenomena in a living cell, the diffusion coefficients and applicable spatial scales are expected to vary between individual specimen. To find the applicable spatial frequency range (λ_{min} and λ_{max} in Fig. 3), we perform an exhaustive search of all possible ranges and apply a metric to eliminate ranges that do not fit the q^2 or q behavior (Fig. 4). Specifically, our algorithm proceeds by choosing a window size (i.e., 3 frequency bins starting at q_1) over which we perform a polynomial fit. The window is then shifted to the next frequency bin (i.e., 3 frequency bins starting at q_2). In this way, the algorithm covers the entire dispersion curve for a particular bin size (Γ for each q). Then the same computation is performed at a larger window size (i.e., 4 frequency bins). This procedure traverses the entire parameter space to extract the diffusion and advection spread for every window size, at every frequency bin (Fig. 4, "initial parameter space"). Our constraint demands that both the linear and quadratic behavior are present simultaneously, such that we infer both the velocity spread and diffusion coefficient. In other words, regions that fit one behavior and yield unphysical values for the second (e.g., either negative diffusion coefficient or negative velocity spread) are eliminated.

The vast majority of such frequency windows and range pairs result in diffusion/advection coefficients that are not valid according to our model (Fig. 4, black area), whereby either one of the coefficients is negative. It is worth noting that the primary reason why pairs are eliminated is the dominance of either advection or diffusion for those size scales (Fig. 4, red area). When one term dominates, a polynomial fit will often have a slight negative coefficient in the other term. Obviously, in these cases one would fit for only advection or diffusion— but not both (as we did). Yet, fitting for only one coefficient is not a viable strategy for dimensionality reduction because then almost all scales would be valid. Instead we investigate both advection and diffusion coefficients, and from this set of valid spatial scales, we apply a constraint that selects for the first large, continuous, spatial scale.
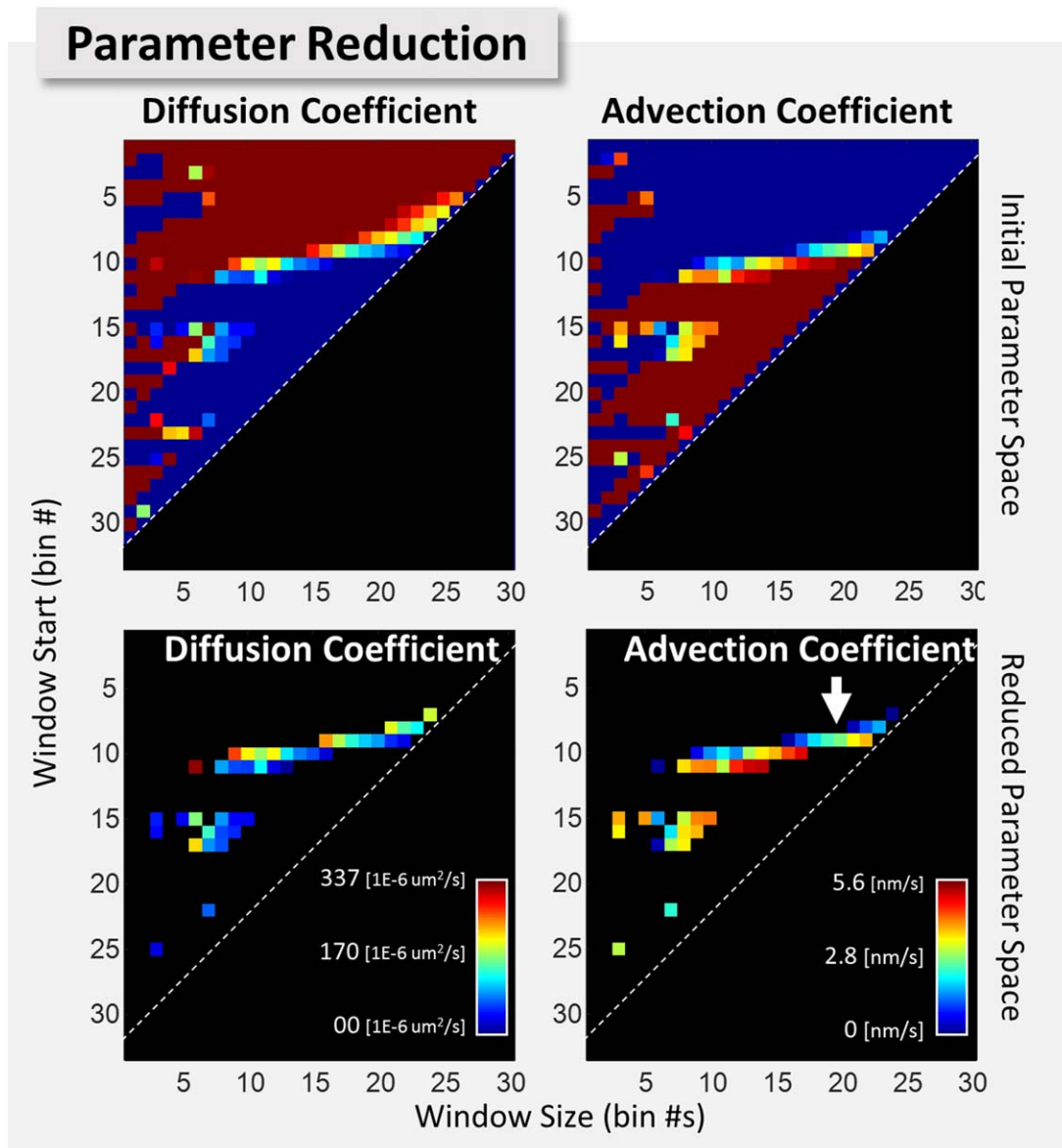
Figure 4. Automatic curve fitting determines the scale characteristic to transport phenomena. In our exhaustive search, the diffusion and advection spread coefficients are calculated for every possible window size and position. Negative coefficient pairs are pruned, resulting in a "reduced parameter space". From this set of valid choices, we automatically select the longest continuous window. In this case we choose a window size of 18 bins starting from frequency window 10, as indicated by the white arrow. [Color figure can be viewed at wileyonlinelibrary.com]

In our implementation, the curve fitting is performed using a QR decomposition as implemented by the Eigen library (21,22). The order of algorithm of the search is approximately $O(1/2n^2)$ where n is a side of the 3D volume. Given the speed of a modern computer and the optimizations afforded by the C++ programing language, an exhaustive search of frequency scales composed of over a thousand elements can be comfortably computed in under a second. A notable outcome of this procedure is the automatic exclusion of data outside the diffraction limit.

In summary, our processing technique reduces a time series of tomographic data, for each cell body or neurite, into two curves representing *XY* and *YZ* motion. These curves are

then automatically analyzed to yield diffusion and advection spread coefficients, characterizing the behavior of the selected region.

RESULTS

An analysis of advection velocities illustrates the advantages of acquiring full-field tomographic data. Looking at the *XY* plane, it appears that the median advection spread is 44% greater in cell bodies compared with nuerites. Yet, a more thorough analysis using the Mann–Whitney *U* test (23) shows that this conclusion is not statistically sound, with a test value of *P* values = 0.12, above the 0.05 threshold for

Table 1. Values of D and Δv

	MEDIAN DIFFUSION COEFFICIENT (1E-6 μm^2/s)	MEDIAN ADVECTION COEFFICIENT (nm/s)
Body (*XY*)	20.6	0.92
Neurite (*XY*)	8.7	0.64
Body (*YZ*)	18.8	1.15
Neurite (*YZ*)	16.9	0.7

Table 2. Degree of difference between transport in cell bodies and neurites

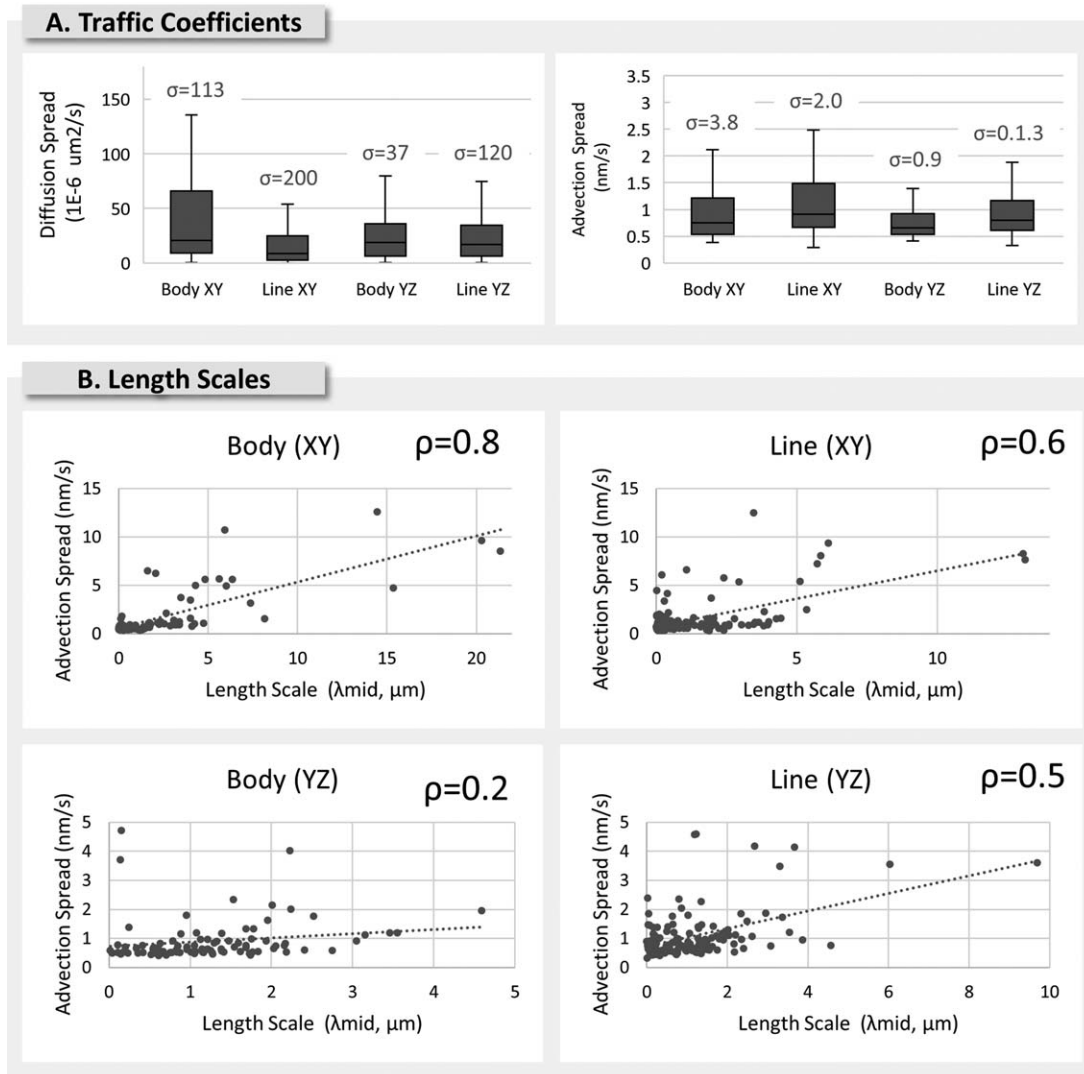|		MANN–WHITNEY *U* TEST [*P*-VALUE]
Diffusion in bodies (*XY*)	Diffusion in neurites (*XY*)	6.07E-5
Diffusion in bodies (*YZ*)	Diffusion in neurites (*YZ*)	0.75
Advection in bodies (*XY*)	Advection in neurites (*XY*)	0.12
Advection in bodies (*YZ*)	Advection in neurites (*YZ*)	0.02

Figure 5. Summary of measured parameters. The diffusion and advection spread coefficients show an overall greater diversity of motion inside cellular bodies (**A**). Furthermore, the associated advection coefficients appear positively correlated with increasing length scales, especially in the case of transport along the horizontal (*XY*) inside cell bodies ($\rho = 0.8$). See discussion in text for detailed analysis.

Table 3. Spatial scales characteristic to each transport regime. See Figure 5

	PEARSON CORRELATION WITH LENGTH SCALE [0–1]
Diffusion in bodies (XY)	0.23
Diffusion in bodies (YZ)	0.05
Diffusion in neurites (XY)	0.40
Diffusion in neurites (YZ)	0.15
Advection in bodies (XY)	0.77
Advection in bodies (YZ)	0.17
Advection in neurites (XY)	0.60
Advection in neurites (YZ)	0.47

claiming a difference. The YZ plane shows a similar trend, 48%, but this conclusion can be made with a much higher confidence (P values = 0.02). It is worth noting that a purely 2D analysis would be unable to detect this difference with a statistically legitimate confidence. A summary of the analysis is present in Table 1 (data) and Table 2 (statistics).

The diffusion coefficients demonstrate how full tomographic imaging can be used to gain new insight into cytology. As shown in Figure 5, the diversity in diffusion/advection coefficients appears much greater inside cellular bodies when compared with the diffusion coefficients in the more restricted extensions. While the median diffusion coefficients along the XY, appears to more than twice as large when comparing the transport inside the more "restricted" neurites to the less "restricted" cell bodies (20.7 vs. 8.7 1E-6 μm^2/s at P values = 6.07E-5). We note that the diffusion phenomena have comparable mangitude in the YZ plane (18.8 vs. 16.8 1E-6 μm^2/s at P values = 0.75). The nearly twice higher diffusion in neuronal extensions in YZ hints that the trajectories of cellular cargo are a lot "bumpier" than previously thought, and that the restriction of cargo transport primarily applies to in-plane motion. Certainly similar diffusion coefficients hint at a similar underlying mechanics.

Building on previous work (24), our automated procedure lets us interrogate the scales associated with the motion that matches our diffusion model. With the exception of vertical transport in cell bodies, there is a strong Pearson product-moment correlation (25) between size scale and the spread of the advection coefficients (ρ in Fig. 5). One interpretation is that larger size scales include cargo that can tolerate a greater diversity of molecular motors, which then leads to a greater diversity in observed speeds (26). Interestingly, no such strong relationship exists for diffusive motion ($\rho < 0.5$), suggesting that this kind of motion is independent of scale (Table 3).

SUMMARY AND DISCUSSION

In summary, with our new analysis method, we are able to investigate cellular transport in three dimensions, providing insight into the intracellular behavior that is otherwise difficult to obtain with fluorescence imaging. It is nevertheless important to stress that quantitative phase imaging is compatible with fluorescent microscopy, and the kind of data shown here could be refined into more precise categories with labels from an epi-fluorescence overlay. For example, a fluorescence channel may reveal the specific traffic inside the neurite.

In this work, the growth cone structure at the neurite tip was purposely avoided as it exhibited vivid motion on a scale that is difficult to capture with our phase-shifting interferometers. We hope that this newfound capability to analyze transport in tomographic volumes will inspire faster imagining system.

DISCLOSURE OF CONFLICTS OF INTEREST

G.P. has a financial interest in Phi Optics, Inc., a company developing quantitative phase imaging technology for materials and life science applications.

LITERATURE CITED

1. Segev N. Trafficking Inside Cells: Pathways, Mechanisms, and Regulation. Austin, TX; New York, NY: Landes Bioscience; Springer Science+Business Media; 2009. 445 p.
2. Magde D, Elson E, Webb WW. Thermodynamic fluctuations in a reacting system—measurement by fluorescence correlation spectroscopy. Phys Rev Lett 1972;29: 705–708.
3. Srivastava M, Petersen NO. Image cross-correlation spectroscopy: A new experimental biophysical approach to measurement of slow diffusion of fluorescent molecules. Methods Cell Sci 1996;18:47–54.
4. Hattori M, Shimizu H, Yokoyama H. Fluorescence correlation spectroscopy with traveling interference fringe excitation. Rev Sci Instrum 1996;67:4064–4071.
5. Hebert B, Costantino S, Wiseman PW. Spatiotemporal image correlation spectroscopy (STICS) theory, verification, and application to protein velocity mapping in living CHO cells. Biophys J 2005;88:3601–3614.
6. Rossow MJ, Sasaki JM, Digman MA, Gratton E. Raster image correlation spectroscopy in live cells. Nat Protoc 2010;5:1761–1774.
7. Meyvis TK, De Smedt SC, Van Oostveldt P, Demeester J. Fluorescence recovery after photobleaching: A versatile tool for mobility and interaction measurements in pharmaceutical research. Pharm Res 1999;16:1153–1162.
8. Popescu G. Quantitative Phase Imaging of Cells and Tissues. McGraw Hill Professional; 2011.
9. Bhaduri B, Kandel M, Brugnara C, Tangella K, Popescu G. Optical assay of erythrocyte function in banked blood. Sci Rep 2014;4:6211–6216.
10. Jang Y, Jang J, Park Y. Dynamic spectroscopic phase microscopy for quantifying hemoglobin concentration and dynamic membrane fluctuation in red blood cells. Opt Express 2012;20:9673–9681.
11. Reed J, Troke JJ, Schmit J, Han S, Teitell MA, Gimzewski JK. Live cell interferometry reveals cellular dynamism during force propagation. ACS Nano 2008;2: 841–846.
12. Ceballos S, Kandel M, Sridharan S, Majeed H, Monroy F, Popescu G. Active intracellular transport in metastatic cells studied by spatial light interference microscopy. J Biomed Opt 2015;20:111209–6.
13. Krizova A, Collakova J, Dostal Z, Kvasnica L, Uhlirova H, Zikmund T, Vesely P, Chmelik R. Dynamic phase differences based on quantitative phase imaging for the objective evaluation of cell behavior. J Biomed Opt 2015;20:111214–8.
14. Wang R, Wang Z, Millet L, Gillette MU, Levine AJ, Popescu G. Dispersion-relation phase spectroscopy of intracellular transport. Opt Express 2011;19: 20571–20579.
15. Beaudoin Iii GMJ, Lee S-H, Singh D, Yuan Y, Ng Y-G, Reichardt LF, Arikkath J. Culturing pyramidal neurons from the early postnatal mouse hippocampus and cortex. Nat Protoc 2012;7:1741–1754.
16. Mattson MP, Kater SB. Isolated hippocampal neurons in cryopreserved long-term cultures: Development of neuroarchitecture and sensitivity to NMDA. Int J Dev Neurosci 1988;6:439–452.

17. Wang Z, Millet L, Mir M, Ding H, Unarunotai S, Rogers J, Gillette MU, Popescu G. Spatial light interference microscopy (SLIM). Opt Express 2011;19:1016–1026.

18. Reynaud EG, Peychl J, Huisken J, Tomancak P. Guide to light-sheet microscopy for adventurous biologists. Nat Methods 2015;12:30–34.

19. Kandel ME, Teng KW, Selvin PR, Popescu G. Label-free imaging of single microtubule dynamics using spatial light interference microscopy. ACS Nano 2017;11:647–655.

20. Semiconductor N. Power Spectra Estimation: Application Note 255. 1980.

21. Heath MT. Scientific Computing: An Introductory Survey. In: Eric MM, editor. McGraw-Hill Higher Education; 1996. 408 p.

22. Eigen V. Guennebaud and Beno.

23. Mann HB, Whitney DR. On a test of whether one of two random variables is stochastically larger than the other. Ann Math Stat 1947;18:50–60.

24. Ceballos S, Kandel M, Sridharan S, Monroy F, Popescu G. Nuclear Dynamics in metastatic cells studied by quantitative phase imaging 2015; Proc SPIE; 9336, Quantitative Phase Imaging 93361Q. DOI: 10.1117/12.2183296. pp 93361Q–93361Q-5.

25. Pearson K. Note on regression and inheritance in the case of two parents. Proc R Soc Lond 1895;58:240–242.

26. Kural C, Kim H, Syed S, Goshima G, Gelfand VI, Selvin PR. Kinesin and dynein move a peroxisome *in vivo*: A tug-of-war or coordinated movement? Science 2005; 308:1469–1472.